Sub-10-nm intracellular bioelectronic probes from nanowire–nanotube heterostructures

Tian-Ming Fu[a], Xiaojie Duan[a,b,1], Zhe Jiang[a], Xiaochuan Dai[a], Ping Xie[a], Zengguang Cheng[a], and Charles M. Lieber[a,c,1]

[a]Department of Chemistry and Chemical Biology, Harvard University, Cambridge, MA 02138; [b]Department of Biomedical Engineering, College of Engineering, Peking University, Beijing 100871, China; and [c]School of Engineering and Applied Sciences, Harvard University, Cambridge, MA 02138

Contributed by Charles M. Lieber, December 17, 2013 (sent for review December 11, 2013)

The miniaturization of bioelectronic intracellular probes with a wide dynamic frequency range can open up opportunities to study biological structures inaccessible by existing methods in a minimally invasive manner. Here, we report the design, fabrication, and demonstration of intracellular bioelectronic devices with probe sizes less than 10 nm. The devices are based on a nanowire–nanotube heterostructure in which a nanowire field-effect transistor detector is synthetically integrated with a nanotube cellular probe. Sub-10-nm nanotube probes were realized by a two-step selective etching approach that reduces the diameter of the nanotube free-end while maintaining a larger diameter at the nanowire detector necessary for mechanical strength and electrical sensitivity. Quasi-static water-gate measurements demonstrated selective device response to solution inside the nanotube, and pulsed measurements together with numerical simulations confirmed the capability to record fast electrophysiological signals. Systematic studies of the probe bandwidth in different ionic concentration solutions revealed the underlying mechanism governing the time response. In addition, the bandwidth effect of phospholipid coatings, which are important for intracellular recording, was investigated and modeled. The robustness of these sub-10-nm bioelectronics probes for intracellular interrogation was verified by optical imaging and recording the transmembrane resting potential of HL-1 cells. These ultrasmall bioelectronic probes enable direct detection of cellular electrical activity with highest spatial resolution achieved to date, and with further integration into larger chip arrays could provide a unique platform for ultra-high-resolution mapping of activity in neural networks and other systems.

nanoelectronics | neural mapping | subcellular | transmembrane potential

Intracellular electrical recording, which can reveal substantially greater details of cellular process compared to extracellular recording, is important for both biological studies and biomedical applications (1–8). Ideally, an intracellular probe should embody two essential characteristics: (*i*) it should be as small as possible to increase spatial resolution, which can provide access to small subcellular structures, and to reduce invasiveness; and (*ii*) it should have a sufficiently large-frequency bandwidth (BW) to record both fast signals related to opening/closing of ion channels (6, 9, 10) and slowly changing or DC signals associated with synaptic interactions (1, 2). Several approaches have been taken to achieve these goals (2, 11). Sharp microelectrodes, which access the cell interior by direct insertion of metal (1, 12) or carbon (13, 14) microelectrodes, and more recently chip-based arrays of vertical metal electrodes (11, 15–17) have been used to record intracellular and intracellularlike signals. Further development of these probes with respect to achieving the above miniaturization goals does, however, face intrinsic limits related to increasing electrode impedance with decreasing size. The patch-clamp micropipette technique also faces constraints for miniaturization related to increasing impedance with probe-size reduction (2, 18).

An alternative approach that can overcome the above limitations of probe-size reduction has focused on using active semiconductor nanowire field-effect transistors (FET) detectors (7, 19, 20), which do not depend on interfacial impedance (21–23). The capability to control synthetically nanowire structure and morphology (24–31) also has enabled hierarchical design of several types of intracellular bioelectronic probes with sizes down to sub-100-nm regime (7, 19, 20). For example, branched intracellular nanotube field-effect transistors (BIT-FETs) (19), which are designed based on a nanowire–nanotube heterostructure, achieve intracellular recording by penetrating the cell membrane with a silicon dioxide (SiO_2) nanotube, thereby bringing the cell cytosol into contact with the underlying (extracellular) silicon nanowire (SiNW) FET detector.

Here we exploit the synthetic flexibility of this bioelectronic probe design to investigate reduction of the SiO_2 nanotube probe an order of magnitude to the sub-10-nm regime, which could open up opportunities to interrogate small subcellular structures and organelles (Fig. 1*A*), and could provide high spatial resolution for mapping. To realize our sub-10-nm bioelectronic probe, there are three challenges that must be addressed. First, nanotube probes and their heterojunction with SiNW FETs will become mechanically less stable as diameter is reduced. Second, the electrical sensitivity will be reduced with decreasing nanotube diameter because the nanotube inner diameter (ID) defines the effective device gate area. Third, high-frequency dynamic response may degrade with decreasing nanotube ID due to increasing solution resistance in the nanotube. Our synthesis, fabrication, and characterization studies described below show how these challenges can be successfully met to realize a functional sub-10-nm bioelectronic probe.

Significance

The miniaturization of bioelectronic probes to enable interrogation of small subcellular structures could impact significantly biology and medicine. This paper describes the design, fabrication, and demonstration of the sub-10-nm bioelectronic devices by exploiting a unique three-dimension nanowire–nanotube structure, where a nanowire detector is synthetically integrated with a nanotube probe. Devices with nanotube probe dimensions as small as 5 nm, which approach the size of a single ion channel, have been realized. Experimental measurements and numerical simulations show that these devices have sufficient time resolution to record the fastest electrical signals in neurons and other cells. Measurement of the cell transmembrane resting potential with these ultrasmall bioelectronic devices further demonstrates their capability for intracellular electrophysiology studies.

Author contributions: T.-M.F., X. Duan, and C.M.L. designed research; T.-M.F., X. Duan, Z.J., and X. Dai performed research; T.-M.F., X. Duan, Z.J., X. Dai, P.X., and C.M.L. analyzed data; P.X. and Z.C. contributed new reagents/analytic tools; and T.-M.F., X. Duan, and C.M.L. wrote the paper.

The authors declare no conflict of interest.

[1]To whom correspondence may be addressed. E-mail: xjduan@pku.edu.cn or cml@cmliris.harvard.edu.

This article contains supporting information at online www.pnas.org/lookup/suppl/doi:10.1073/pnas.1323389111/-/DCSupplemental.

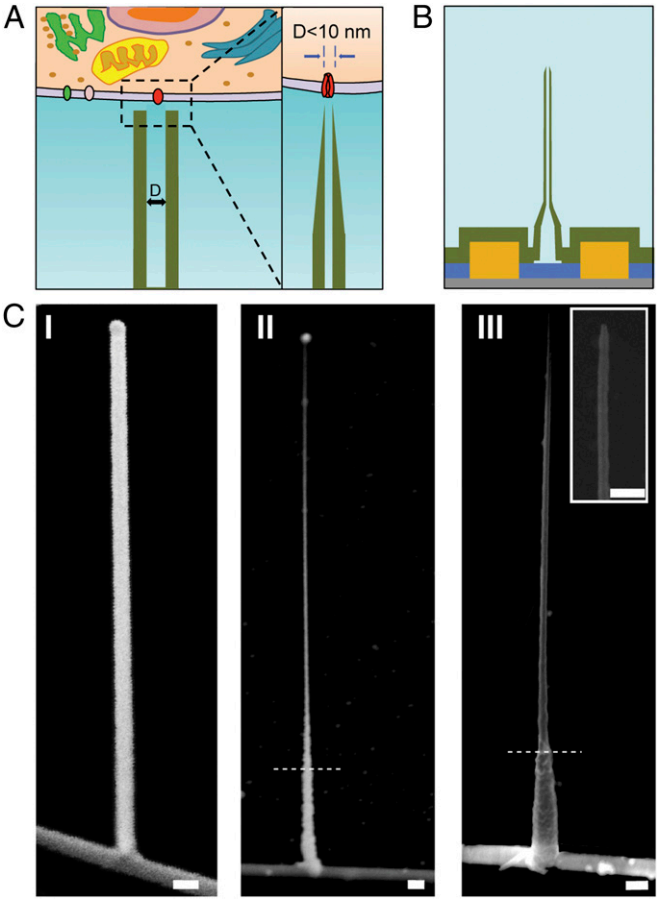

Fig. 1. Schematics and SEM images of the ultrasmall BIT-FET. (*A*) Schematic illustration of an intracellular bioelectronic probe. (*Left*) General scheme of a probe for intracellular electrophysiology recording. (*Right*) A magnified view of the tip of a sub-10-nm bioelectronic probe and its related size to single ion channel. (*B*) Schematic structure of the ultrasmall BIT-FET. Green, yellow, blue, and gray colors represent SiO_2 layer, metal contact, SiNW, and silicon nitride substrate, respectively. (*C*) SEM images of the ultrasmall BIT-FET at different fabrication steps. A GeNW branch was first grown on top of SiNW (*I*), followed by a subsequent H_2O_2 etching of top part of GeNW to shrink its diameter down to sub-10-nm regime (*II*). A final view of an ultrasmall BIT-FET with nanotube ID ~8 nm, and SiO_2 wall thickness ~10 nm is presented in (*III*). *Inset* of *III* is the closeup of the tip of the ultrasmall SiO_2 nanotube. White dashed lines in *II* and *III* indicate the point below which the GeNW and SiO_2 is protected by photoresist during H_2O_2 and BHF etching, respectively. All scale bars: 100 nm.

Results and Discussion

Our target for the ultrasmall BIT-FET incorporating a sub-10-nm nanotube probe (Fig. 1 *A* and *B*) has several key features to enable sufficient mechanical strength and electrical sensitivity as follows. First, the nanotube probe has a long free-end with small ID and thin wall for facile and minimally invasive cell penetration. Second, a much larger ID and thicker wall are used for the bottom part of the nanotube to provide mechanical stability and increase the effective gate area of the SiNW FET detector. This latter feature can also ensure high electrical sensitivity of the bioelectronic probe.

To realize this target device structure we developed an efficient multistep synthesis and fabrication approach (Fig. 1*C*, Figs. S1 and S2, and *SI Text*). First, SiNW FETs were fabricated on a substrate surface (Fig. S1 *A* and *B*) using previously established methods (25). Second, germanium nanowire (GeNW) branches, which serve as sacrificial templates for the nanotube probes (19), were grown on top of the SiNW FETs via our gold-nanoparticle–catalyzed method (26) with the nanoparticle position precisely defined by electron-beam lithography between the source and drain (S/D) electrodes of the FET (Fig. S1 *C* and *D*). A representative scanning electron microscopy (SEM) image shows a nearly vertical GeNW grown from the upper surface of the SiNW (Fig. 1*C, I*). Third, selective hydrogen peroxide (H_2O_2) etching was carried out to reduce the size of the upper portions of the GeNWs while the lower portions of the GeNWs, where they connect to the SiNWs, are protected by a thin photoresist layer with thickness about 20% of the entire GeNW length (Fig. S1 *E* and *F*). A typical SEM image (Fig. 1*C*, *II*) shows that this selective etching step yields GeNWs with diameters <10 nm for the upper portions and diameters ca. 80–90 nm for the lower portions. The larger diameter for the lower portion enhances the mechanical strength of the structure, and together with the Ge shell deposited on the SiNW (simultaneously with GeNW growth), is also important to the overall device sensitivity as discussed below.

To form the nanotube structure, a thin ca. 30 nm SiO_2 layer was conformally deposited by atomic-layer deposition (ALD) on the SiNW-branched GeNW heterostructures and entire device substrate (Figs. S1*G* and S2*A*). In addition to coating the GeNW, this ALD process deposits the same thickness SiO_2 on the SiNW FET and S/D electrodes, and thus serves to passivate (i.e., isolate) these structures from solution in our experiments. Selective buffered hydrofluoric acid (BHF) etching was then carried out to reduce the thickness of upper SiO_2 shell to ~10 nm and the lower portion of the shell was protected by photoresist (Figs. S1 *H* and *I* and S2*A*). To complete the device structure, a two-step etching process was carried out in a manner similar to that described previously for the conventional BIT-FET (20). First, the upper tip of the Ge core was exposed by removing the SiO_2 shell using BHF, and then the GeNW was removed using H_2O_2. A representative SEM image of an ultrasmall BIT-FET (Fig. 1*C*, *III*) shows several key features. First, the upper portion of the SiO_2 nanotube has an ID of ~8 nm and a wall thickness of ~10 nm. Second, the very tip of the nanotube is tapered due to BHF etching yielding a relative sharp point for insertion. Third, the lower portion of the nanotube has much larger ~80-nm ID and 30-nm wall thickness as expected based on our fabrication process. In addition, transmission electron microscopy (TEM) images (Fig. S2*B*) confirm the ultrasmall IDs of the upper portions of the SiO_2 nanotubes.

The basic electrical sensitivity of the ultrasmall BIT-FET devices before and after GeNW etching was characterized using standard quasi-static water-gate measurements (19, 32) (*SI Text*). Representative device conductance, G, versus applied water-gate voltage, V_{wg}, data (Fig. 2*A*) shows that G changes very little as a function of V_{wg} before GeNW etching, but exhibits a large change after GeNW etching to form the nanotube structure. Indeed, the magnitude of the transconductance (device sensitivity) increases from 0.24 to 2.75 μS/V after etching. In addition, control measurements performed on SiNW FET devices without nanotubes or GeNW branches exhibit no increase in transconductance after etching similar to previous studies (19). Together, these results confirm that solution can fill a small SiO_2 nanotubes, and that the SiNW FET detector responds selectively to the solution inside the nanotubes versus outside.

The enhanced sensitivity following GeNW etching to form the nanotube probe structure reflects two key contributions. First, the solution gates the SiNW FET via a much thinner (1–2 nm native oxide) SiO_2 versus 30 nm deposited layer before GeNW etching. Second, the Ge layer deposited on the SiNW FET during GeNW growth is etched during nanotube formation process to yield an effective gate area that is much larger than that defined by the nanotube ID (Fig. 1*B* and Fig. S3).

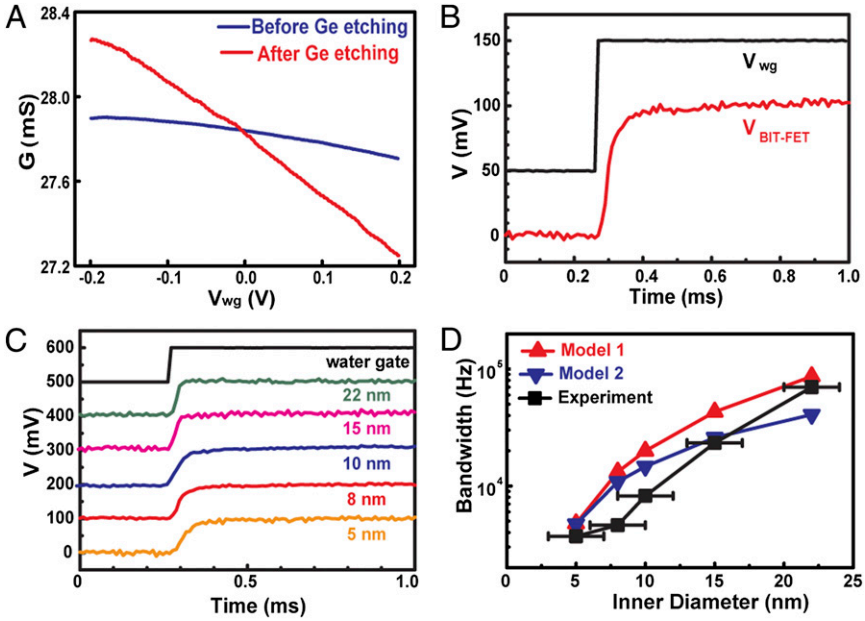

Fig. 2. Water-gate characterization and BW measurements. (*A*) Conductance *G* of an ultrasmall BIT-FET with ~7 nm ID versus water-gate voltage V_{wg} before (blue) and after (red) core GeNW etching. (*B*) A step water-gate pulse V_{wg} with 0.01-ms rise time and 100-mV steady-state amplitude (black) and the corresponding response from a typical ultrasmall BIT-FET with ~10 nm nanotube ID and 3.2 μm length (red). Response from metal contacts has been removed (Fig. S4). The recorded voltage signal is calibrated by the device transconductance measured from quasi-static water-gate experiment; V_{wg} and V_{signal} are offset by 50 mV for clarity. (*C*) Step-pulsed water-gate responses from ultra-small BIT-FETs with different nanotube IDs. Same voltage calibration was adopted as *B*. Traces are offset by 100 mV for clarity. (*D*) Measured BW of ultrasmall BIT-FET devices versus the ID of the nanotube and comparison with numerically calculated data. Models 1 and 2 present the upper (the active gate area is defined by the nanotube ID) and the lower limit (the entire SiNW surface is active) of the device (*SI Text*). For comparison, all of the BWs were normalized to a uniform nanotube length of 2.5 μm. Due to the equipment BW limit, the BW of the 22-nm device is extrapolated from its BW in 0.1x PBS solution by taking the relative conductivity of 1x PBS and 0.1x PBS into account (*SI Text*). The error bar corresponding to the SE of the experimental data are ±2 nm induced by SEM measurement uncertainty. All of the devices for experiment and modeling have a top nanotube wall thickness ~10 nm.

We characterized the BW of the ultrasmall BIT-FETs through step water-gate pulse measurements in 1x phosphate buffered saline (1x PBS) solution (*SI Text*) to define further their capabilities for electrophysiological recording in cells. The temporal response of a device with 10-nm ID nanotube following a steplike water-gate pulse (rise time = 0.01 ms, amplitude = 100 mV) is shown in Fig. 2*B*, where the capacitive coupling from the metal contacts was removed (Fig. S4) and the measured conductance change was

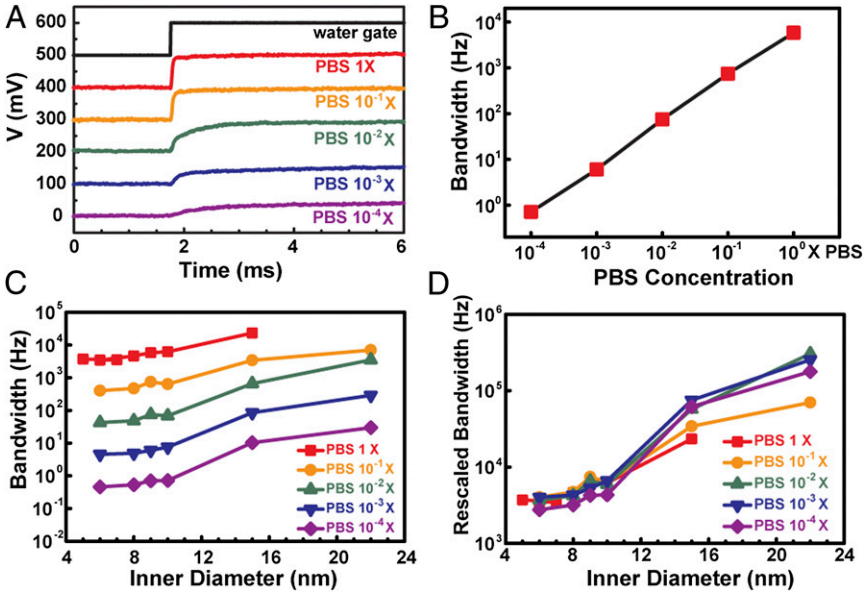

Fig. 3. Device bandwidth dependence on electrolyte concentration. (*A*, *B*) Pulsed water-gate responses (traces offset by 100 mV) and corresponding BWs of a ~10 nm nanotube ID ultrasmall BIT-FET in solutions with different PBS concentration. (*C*) Measured BWs of ultrasmall BIT-FET devices versus nanotube ID in different concentration PBS solutions. (*D*) Rescaled device BWs versus nanotube ID. All BWs are rescaled by solution resistivity (*SI Text*).

converted to voltage using the device sensitivity (32). Qualitatively, the recorded data exhibits a slower time response (i.e., rounding with respect to water-gate voltage step), which indicates that the probe's time response is slower than 0.01-ms rise time of the applied voltage step. Following previous studies (19), we can define the effective BW as

$$BW = \frac{0.35}{t_{90\%} - t_{10\%}}, \quad [1]$$

where $t_{90\%} - t_{10\%}$ is the time needed for the recorded signal to change from 10 to 90% of the steady-state amplitude of the applied V_{wg}. Analysis of the data in Fig. 2*B*, where $t_{90\%} - t_{10\%} =$ 58 μs, yield a BW of ~6.0 kHz.

To further elucidate the nanotube ID dependence of the ultrasmall BIT-FETs BW, we carried out similar pulsed water-gate measurements for ultrasmall BIT-FET devices with different nanotube IDs. The measured calibrated voltage signal as a function of time data for devices with nanotube IDs from 5 to 22 nm (Fig. 2*C*) shows that the rise time for the recorded signal to reach 100-mV steady-state increases as the nanotube ID decreases. Quantitatively, the calculated BW of each probe based on Eq. **1** is shown in Fig. 2*D*. These data show that BW decreases from ca. 88 to 3.1 kHz as the nanotube ID decreases from 22 to 5 nm, respectively.

To gain further insight into the measured data we also modeled the ultrasmall BIT-FET BW (Fig. S5*A*). The time evolution of the potential at the SiNW FET surface following a steplike pulsed water-gate potential was numerically evaluated (*SI Text*) for two different models. The upper BW limit (model 1) assumes the active gate area is defined by the nanotube ID (e.g., Fig. S3*A*), and the lower BW limit (model 2) assumes that the entire SiNW surface is active (i.e., the deposited Ge layer is etched over the SiNW surface as shown schematically in Fig. S3*B*). The calculated BW results for the two models (Fig. 2*D*) are consistent with the experimental data, although somewhat overestimates BW at the smaller diameters. This difference can be attributed to a larger gap over the SiNW FET detector (Fig. S3*B*) than used in model 2, although future studies will be required to understand fully these differences. It is important to note that the measured and calculated BW values for the smallest 5-nm ID nanotube probes, 3.1 kHz, are sufficient to enable accurate recording of most fast dynamic cellular processes.

We have further characterized the BW of the ultrasmall BIT-FETs in different ionic strength PBS solutions. Representative data recorded following a water-gate potential step using an ultrasmall BIT-FET with 10-nm ID nanotube (Fig. 3*A*) exhibit a clear increase of rise time with decreasing solution concentration. A plot of the BW versus solution concentration determined from this data (Fig. 3*B*) shows that the BW depends linearly on PBS concentration. Qualitatively, this behavior is consistent with our model given the expected dependence of BW on solution resistivity.

We have further explored this dependence by recording the time response from ultrasmall BIT-FETs with different nanotube IDs in different concentration PBS solutions, where the resulting BW results are summarized in Fig. 3*C*. In addition, these results were rescaled by normalizing the solution resistivity to that in 1x PBS (Fig. 3*D*); that is, multiplying the BW by $\rho_{sol}/\rho_{1x\ PBS}$, where ρ_{sol} and $\rho_{1x\ PBS}$ are the resistivity of the solution and 1x PBS solution, respectively. The rescaled data exhibits a nearly universal dependence on nanotube ID, where we attribute deviations to contributions from the tip access impedance and capacitive coupling to the underlying SiNW FET. These latter factors become more prominent for larger ID nanotube devices, although we assume that the BW is dominated only by the nanotube in our analysis. We have also used a simplified analytical model to obtain additional insight into the device behavior (*SI Text*). Specifically, this analysis provides an explicit relationship for the BW as a function of solution resistivity inside the nanotube (inverse), the nanotube wall capacitance per unit length (inverse) and nanotube length (inverse square), and thus also can be used to guide the design of ultrasmall BIT-FETs to achieve required BWs.

The ultrasmall BIT-FET nanotubes are coated with phospholipid layers to facilitate the cell-membrane penetration for intracellular recording (7, 19, 20, 33–36). Because the smallest nanotube IDs investigated in our studies approach the thickness of phospholipid bilayer ~4.75 nm (37), we measured the BWs of several probes before and after phospholipid modification (*Materials and Methods*). Analysis of data recorded with an ultrasmall BIT-FET having a 10-nm ID and 2.8-μm-long nanotube (Fig. 4*A*) shows that the BW dropped from 9.7 to 3.0 kHz after

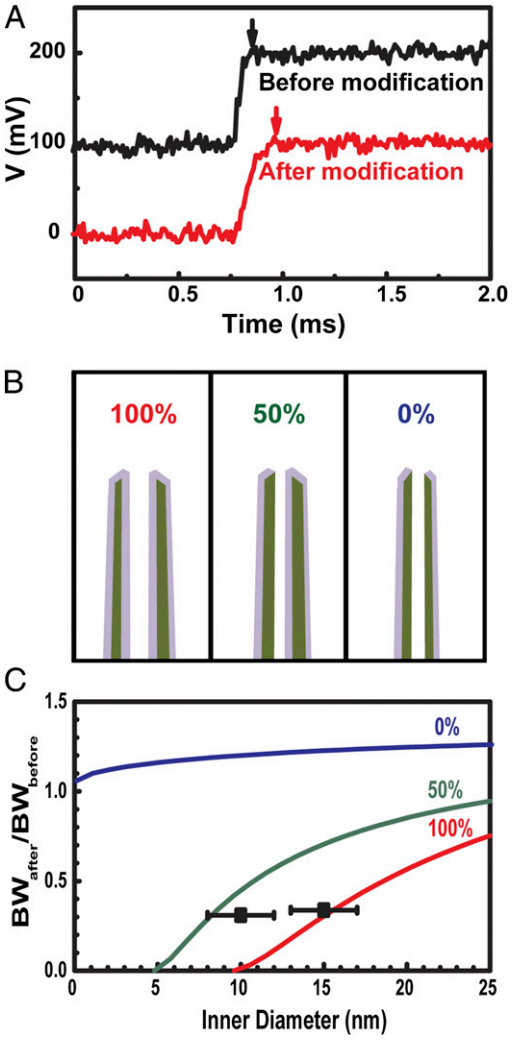

Fig. 4. Device bandwidth after phospholipid modification. (*A*) Pulsed water-gate responses from a ~10 nm nanotube ID ultrasmall BIT-FET before (black) and after (red) phospholipid modification. The black and red arrows indicate the points when the curves reach steady-state amplitudes. Traces are offset by 100 mV for clarity. (*B*) Schematics of three possible scenarios for phospholipid modification: both (inner and outer) surfaces of the nanotube are fully covered (*Left*), outer surface is fully covered and inner surface is only 50% covered (*Middle*), and only outer surface is covered (*Right*). The purple and green colors are phospholipid bilayer and SiO_2 nanotube, respectively. (*C*) Calculated ratio of the device BW after and before phospholipid modification versus nanotube ID under different scenarios depicted in *A* (*SI Text*). For comparison, two experimental data are presented (black square).

phospholipid modification and the device sensitivity remained essentially unchanged (<1% variation in transconductance).

To explain the observed reduction in BW in this and other measurements following phospholipid modification, we considered the three scenarios shown schematically in Fig. 4*B*: (case 1) the entire inner and outer surfaces of the nanotube are covered by a lipid bilayer; (case 2) a phospholipid bilayer covers 50% of the inner and all of the outer surfaces of the nanotube; and (case 3) the lipid bilayer is excluded from the inner surface but covers all of the outer surface of the nanotube. The calculated (*SI Text*) BW change expressed as a ratio after/before phospholipid modification for these three scenarios as a function of nanotube ID (Fig. 4*C*) highlights several key points. First, the BW ratio approaches zero for case 1 and case 2 as the nanotube ID approaches the thickness of the bilayer coatings due to the increasing effective solution resistivity. Second and for case 3, the ratio is >1 because of a reduction in effective capacitance of the nanotube. In addition, comparison of these calculations to experimental results for 15- and 10-nm ID nanotube probes (Fig. 4*C*) shows that the experimental BW ratios are close to case 1 and case 2, respectively. In the future, systematic experimental studies should give insight to the control of phospholipid modification to minimize coating of the inner nanotube wall while maintaining coverage of the outer surface to facilitate probe penetration through cell membranes, although we note that the BW drops on modification still yield sufficiently high BWs for 10-nm ID nanotubes to record submillisecond cellular processes such as neuronal action potentials (2, 3, 11).

Last, we have investigated the capability of the ultrasmall BIT-FET for intracellular recording in studies of isolated HL-1 cells (38). A series of differential interference contrast optical microscopy images recorded while moving a single HL-1 cell with a glass micropipette to/from a phospholipid modified ultrasmall BIT-FET with 10-nm ID nanotube probe (Fig. 5*A*) shows several features. First, the substantial size difference between the ultrasmall BIT-FET and glass micropipette is obvious in the images. Second, the nanotube probe can readily penetrate the cell membrane without affecting the overall cell shape, which suggests a biomimetic internalization assisted by lipid modification and hence a reasonably tight seal around the nanotube. Third, when the cell is retracted from the nanotube probe there is no change in cell shape indicating that the membrane readily reseals.

Significantly, measurement of the potential (mV) during the HL-1 cell approach/penetration/retraction process with an independent ultrasmall BIT-FET (Fig. 5*B*) shows (*i*) a stable baseline before contact; (*ii*) a sharp ca. 59-mV drop when the HL-1 cell was brought into contact with the ultrasmall nanotube, which corresponds to the intracellular potential of the cell; and (*iii*) abrupt (within ~300 ms) return to baseline coincident with retraction of the HL-1 cell from the device. These data demonstrate that the ultrasmall BIT-FET can record intracellular potentials, and moreover, can record both low-frequency (shown here) and high-frequency (described above) signals. The capability to record signals over a broad frequency range using 10-nm-scale probe represents a clear advantage of the active ultrasmall BIT-FET device over conventional passive electrodes.

Conclusions

We have designed, fabricated, and demonstrated an ultrasmall intracellular bioelectronic probe, the ultrasmall BIT-FET, based on a nanowire-nanotube heterostructure with probe nanotubes having IDs as small as 5 nm. Systematic studies of the ultrasmall BIT-FET BW through pulsed water-gate measurements and theoretical modeling showed the capability to record fast, submillisecond physiological signals with the smallest ID nanotube probes. Moreover, the effect of phospholipid coatings, which are important for intracellular recording, on probe performance has been characterized and modeled. Importantly, optical microscopy and electrical recording measurements demonstrate that ultrasmall BIT-FET nanotube probes can penetrate and subsequently be retracted from HL-1 cells in minimally invasive manner while continuously recording the transition between extracellular and intracellular rest potential. The ultrasmall BIT-FET opens up unique opportunities for future electrophysiological researches, including intracellular recordings from small subcellular structures and intracellular organelles, such as dendrites, dendritic spines,

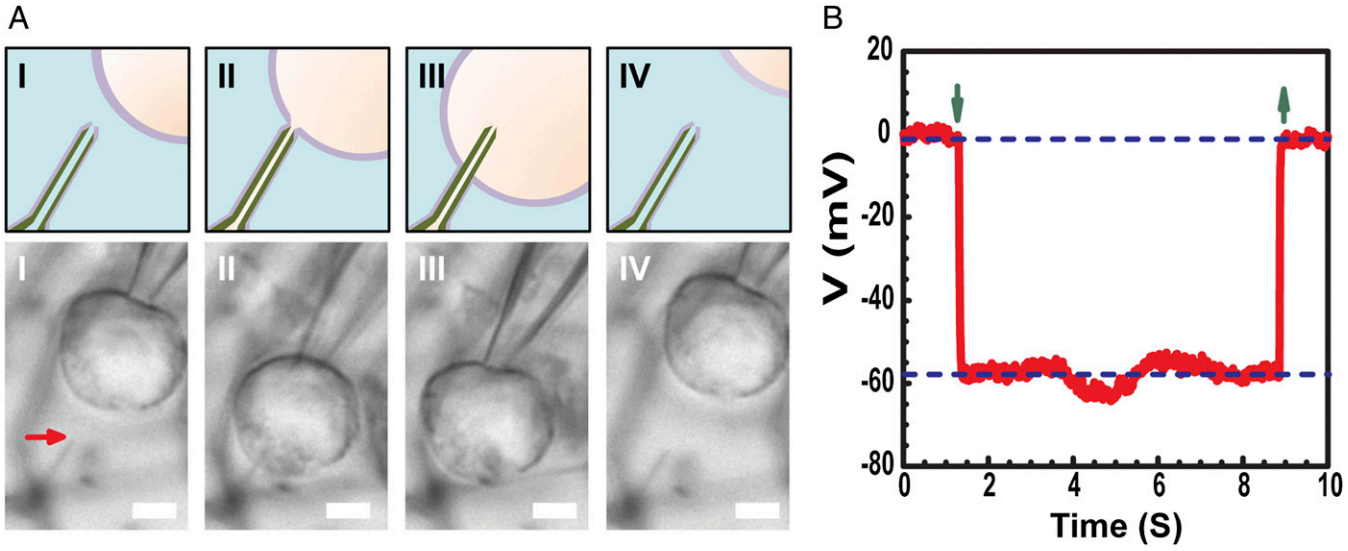

Fig. 5. Intracellular resting membrane potential recording. (*A*) Schematics (*Upper*) and differential interference contrast optical microscopy images (*Lower*) of an HL-1 cell manipulated by a glass micropipette to approach (*I*), contact (*II*), penetrate (*III*), and retract (*IV*) from a phospholipid-modified ultrasmall BIT-FET probe. The red arrow indicates the position of the ultrasmall nanotube tip. Because pure SiO_2 nanotube is optically transparent, the GeNW template of this device was not etched for imaging. Scale bar: 2 μm. (*B*) Representative electrical recording results from a ~10 nm ID ultrasmall BIT-FET device; in this case, the GeNW was etched to yield the ultrasmall SiO_2 nanotube. Down- and up-pointing green arrows mark the beginning of cell penetration and withdrawal, respectively. The upper and lower horizontal dashed lines indicate the extracellular and intracellular potentials. Quasi-static water-gate measurements made before/after cell measurements show <2% change in the device conductance and sensitivity.

and the cell nucleus. Integration of such probes into large-scale arrays could also enable mapping of electrical activity from neural networks with substantially greater spatial resolution and minimal invasiveness than possible with techniques now available.

Materials and Methods

Nanowire Synthesis and Device Fabrication. Key steps in nanowire synthesis and device fabrication are described in *SI Text* and Fig. S1. First, single-crystalline SiNWs were synthesized using the Au nanocluster-catalyzed vapor–liquid–solid growth methodology in a home-built chemical vapor deposition (CVD) system (17). Second, SiNW FETs were fabricated on Si_3N_4-covered Si wafers. Third, GeNWs were grown on top of SiNW FETs using the same CVD system, and the upper portions of the GeNWs were etched in hydrogen peroxide (H_2O_2) solution to reduce their diameters to the 10-nm regime. Fourth, a 30-nm-thick SiO_2 layer was conformally deposited by ALD and then selective BHF etching was used to reduce the upper portion of the SiO_2 layer down to ca. 10-nm thickness. Finally, the tip SiO_2 was removed by BHF and the GeNW core was removed by H_2O_2 etching to form the nanotube probe.

Device Characterization. Two types of water-gate characterization measurements were carried out to elucidate the behavior of the ultrasmall BIT-FET in aqueous solution: (*i*) Standard quasi-static water-gate measurements were made in 1x PBS to determine device sensitivity. (*ii*) A steplike pulsed water-gate measurement was used to characterize the BW of the ultrasmall BIT-FET in different concentration PBS solutions. The details of each measurement are described in *SI Text*.

Phospholipid Modification. SiO_2 nanotubes with negatively charged surfaces were incubated with lipid vesicles of 1,2-dimyristoyl-snglycero-3-phosphocholine (DMPC; Avanti Polar Lipids, Inc.) containing 1% 1-myristoy1-2-{12-[(7-nitro-2–1,3-benzoxadiazol-4-yl)] amino dodecanoyl}-sn-glycero-3-phosphocholine (NBD-lipid; Avanti Polar Lipids, Inc.) as fluorescent reporter to form supported lipid layers. The detailed procedure for this modification process was described in previous literature (7, 36). Fluorescence microscopy images of dye-labeled DMPC modified ultrasmall BIT-FETs were carried out each time after modification to ensure the lipid bilayers form a continuous shell on the SiO_2 nanotube.

Cell Recordings. HL-1 cell culture and phospholipid modification of device chips were carried out following reported methods (7, 19). Transmembrane recording and cell manipulation were carried out in Tyrode solution (pH ~7.3) with a 100-mV DC source voltage at 37 °C. The recording current was amplified with a home-built multichannel current/voltage preamplifier, filtered with a 500-Hz low-pass filter (CyberAmp 380), and digitized at a 50-kHz sampling rate (Axon Digi1440A). Ag/AgCl electrodes were used to fix the extracellular solution potential.

ACKNOWLEDGMENTS. The authors thank M. Mankin for assistance in TEM imaging and H. S. Choe, J. Liu, C. Xie, R. Gao, R. Day, and J. Huang for helpful discussions. X. Duan acknowledges the support from the National Natural Science Foundation of China (21373013), and the National Basic Research Program of China (2014CB932500). C.M.L. acknowledges support of this research from Department of Defense, National Security Science and Engineering Faculty Fellowships (N00244-09-1-0078) Award.

1. Purves RD (1981) *Microelectrode methods for intracellular recording and ionophoresis* (Academic Press, London).
2. Molleman A (2003) *Patch clamping: An introductory guide to patch clamp electrophysiology* (John Wiley, New York).
3. Erickson J, Tooker A, Tai YC, Pine J (2008) Caged neuron MEA: A system for long-term investigation of cultured neural network connectivity. *J Neurosci Methods* 175(1): 1–16.
4. Voelker M, Fromherz P (2005) Signal transmission from individual mammalian nerve cell to field-effect transistor. *Small* 1(2):206–210.
5. Hille B (2001) *Ion channels of excitable membranes* (Sinauer, Sunderland, Mass), 3rd Ed.
6. Dunlop J, Bowlby M, Peri R, Vasilyev D, Arias R (2008) High-throughput electrophysiology: An emerging paradigm for ion-channel screening and physiology. *Nat Rev Drug Discov* 7(4):358–368.
7. Tian BZ, et al. (2010) Three-dimensional, flexible nanoscale field-effect transistors as localized bioprobes. *Science* 329(5993):830–834.
8. Duan XJ, Fu TM, Liu J, Lieber CM (2013) Nanoelectronics-biology frontier: From nanoscopic probes for action potential recording in live cells to three-dimensional cyborg tissues. *Nano Today* 8(4):351–373.
9. Meyer T, Boven KH, Gunther E, Fejtl M (2004) Micro-electrode arrays in cardiac safety pharmacology: A novel tool to study QT interval prolongation. *Drug Saf* 27(11): 763–772.
10. Zheng W, Spencer RH, Kiss L (2004) High throughput assay technologies for ion channel drug discovery. *Assay Drug Dev Technol* 2(5):543–552.
11. Spira ME, Hai A (2013) Multi-electrode array technologies for neuroscience and cardiology. *Nat Nanotechnol* 8(2):83–94.
12. Hubel DH (1957) Tungsten microelectrode for recording from single units. *Science* 125(3247):549–550.
13. Schrlau MG, Dun NJ, Bau HH (2009) Cell electrophysiology with carbon nanopipettes. *ACS Nano* 3(3):563–568.
14. de Asis ED, Jr., Leung J, Wood S, Nguyen CV (2010) Empirical study of unipolar and bipolar configurations using high resolution single multi-walled carbon nanotube electrodes for electrophysiological probing of electrically excitable cells. *Nanotechnology* 21(12):125101.
15. Robinson JT, et al. (2012) Vertical nanowire electrode arrays as a scalable platform for intracellular interfacing to neuronal circuits. *Nat Nanotechnol* 7(3):180–184.
16. Xie C, Lin ZL, Hanson L, Cui Y, Cui BX (2012) Intracellular recording of action potentials by nanopillar electroporation. *Nat Nanotechnol* 7(3):185–190.
17. Hai A, et al. (2009) Changing gears from chemical adhesion of cells to flat substrata toward engulfment of micro-protrusions by active mechanisms. *J Neural Eng* 6(6): 066009.
18. Sakmann B, Neher E (1984) Patch clamp techniques for studying ionic channels in excitable membranes. *Annu Rev Physiol* 46:455–472.
19. Duan XJ, et al. (2012) Intracellular recordings of action potentials by an extracellular nanoscale field-effect transistor. *Nat Nanotechnol* 7(3):174–179.
20. Gao RX, et al. (2012) Outside looking in: Nanotube transistor intracellular sensors. *Nano Lett* 12(6):3329–3333.
21. Sze SM (1982) Citation classic - Physics of semiconductor-devices. *Eng Tech Appl Sci* (27):28.
22. Patolsky F, Zheng GF, Lieber CM (2006) Nanowire-based biosensors. *Anal Chem* 78(13):4260–4269.
23. Misra N, et al. (2009) Bioelectronic silicon nanowire devices using functional membrane proteins. *Proc Natl Acad Sci USA* 106(33):13780–13784.
24. Morales AM, Lieber CM (1998) A laser ablation method for the synthesis of crystalline semiconductor nanowires. *Science* 279(5348):208–211.
25. Cui Y, Wei QQ, Park HK, Lieber CM (2001) Nanowire nanosensors for highly sensitive and selective detection of biological and chemical species. *Science* 293(5533): 1289–1292.
26. Lauhon LJ, Gudiksen MS, Wang D, Lieber CM (2002) Epitaxial core-shell and core-multishell nanowire heterostructures. *Nature* 420(6911):57–61.
27. Wu Y, Xiang J, Yang C, Lu W, Lieber CM (2004) Single-crystal metallic nanowires and metal/semiconductor nanowire heterostructures. *Nature* 430(7000):704.
28. Yang C, Zhong ZH, Lieber CM (2005) Encoding electronic properties by synthesis of axial modulation-doped silicon nanowires. *Science* 310(5752):1304–1307.
29. Lu W, Xiang J, Timko BP, Wu Y, Lieber CM (2005) One-dimensional hole gas in germanium/silicon nanowire heterostructures. *Proc Natl Acad Sci USA* 102(29):10046–10051.
30. Tian BZ, et al. (2007) Coaxial silicon nanowires as solar cells and nanoelectronic power sources. *Nature* 449(7164):885–889.
31. Kempa TJ, et al. (2012) Coaxial multishell nanowires with high-quality electronic interfaces and tunable optical cavities for ultrathin photovoltaics. *Proc Natl Acad Sci USA* 109(5):1407–1412.
32. Patolsky F, Zheng GF, Lieber CM (2006) Fabrication of silicon nanowire devices for ultrasensitive, label-free, real-time detection of biological and chemical species. *Nat Protoc* 1(4):1711–1724.
33. Chernomordik LV, Kozlov MM (2008) Mechanics of membrane fusion. *Nat Struct Mol Biol* 15(7):675–683.
34. VanDersarl JJ, Xu AM, Melosh NA (2012) Nanostraws for direct fluidic intracellular access. *Nano Lett* 12(8):3881–3886.
35. Almquist BD, Melosh NA (2010) Fusion of biomimetic stealth probes into lipid bilayer cores. *Proc Natl Acad Sci USA* 107(13):5815–5820.
36. Huang SC, et al. (2007) Formation, stability, and mobility of one-dimensional lipid bilayers on polysilicon nanowires. *Nano Lett* 7(11):3355–3359.
37. Stern HA, Feller SE (2003) Calculation of the dielectric permittivity profile for a nonuniform system: Application to a lipid bilayer simulation. *J Chem Phys* 118(7): 3401–3412.
38. Claycomb WC, et al. (1998) HL-1 cells: A cardiac muscle cell line that contracts and retains phenotypic characteristics of the adult cardiomyocyte. *Proc Natl Acad Sci USA* 95(6):2979–2984.